

Rhythms of the collective brain: Metastable synchronization and cross-scale interactions in connected multitudes

Miguel Aguilera^{1,2,*}

¹Department of Computer Science and Systems Engineering, University of Zaragoza, Zaragoza, 50018, Spain

²Department of Psychology, University of the Balearic Islands, Palma de Mallorca, 07122, Spain

*sci@maguilera.net

ABSTRACT

Crowd behaviour challenges our fundamental understanding of social phenomena. Involving complex interactions between multiple organizational levels and spanning a variety of temporal and spatial scales of activity, its governing mechanisms defy conventional analysis. Using a data set comprising 1.5 million Twitter messages from the 15M movement in Spain as an example of multitudinous self-organization, we investigate the processes that underlie the coordination its spatial and temporal scales. We propose a generic description of the coordination dynamics of the system measuring phase-locking statistics at different frequencies using wavelet transforms, identifying 8 frequency bands of entrained oscillations between 15 geographical urban nodes. Then we apply maximum entropy inference methods to describe Ising models capturing transient synchrony between geographical nodes in our data at each frequency band. The models show that 1) all frequency bands of the system are operating near critical points of their parameter space and 2) while fast frequencies present only a few metastable states displaying all-or-none synchronization, slow frequencies present a diversity of metastable states of partial synchronization. Furthermore, describing the state at each frequency band using the energy landscape of the corresponding Ising model, we compute transfer entropy to characterize cross-scale interactions between frequency bands, showing 1) a cascade of upward information flows in which each frequency band influences its contiguous slower bands and 2) downward information flows where slow frequencies modulate distant fast frequencies.

Introduction

Coordinated activity is a powerful force in creating and maintaining social ties [1]. From communal dances in ancient human groups to civic festivals in the French Revolution or collective muscular manifestations in Nazi marches and rallies [1, p.136, p.148-149], visceral, emotional sensations of shared movement have been used to create communal identities and to shape political landscapes. Historically, forms of distributed communication and coordination have often come together with episodes of large-scale mobilization and social change, as the widespread print-shop networks of radical reforming movements with the generalization of the printing press during the 16th century German Reformation [2] or postal networks of the Republic of Letters in the Age of Enlightenment a century later [3]. Today, amidst unprecedented development of communication technologies, new forms of coordination for large and scattered communities have been unleashed around the globe.

The rise of new digital communication tools and network technologies is accelerating fast bidirectional communication, generating new forms of collective communication and action. Digital communications increase the autonomy and influence of the social groups using them facilitating forms of mass self-communication [4], collective intelligence using pools of social knowledge [5] or *smart mobs* exploiting new found communication and computing capabilities via ubiquitous devices [6]. From protest movements including the Arab Spring or the Occupy movements to autonomous responses in the face of natural disasters, for example Hurricane Sandy or the Tōhoku earthquake, several examples highlight the increasing power of digitally connected social and political grassroots movements to shape events. Recognition of a growing influence has brought with it heightened scholarly interest in its explanation: how such movements arise and self-organize, what mechanisms underlie their formation and how are they able to constitute autonomous social and political subjects? [7]. Recent advances have described specific elements of connected multitudes: the geographical diffusion of trends [8]; the interplay between exogenous and endogenous dynamics [9]; or the connection between social media and collective activity in physical spaces [10]. Nevertheless, many of the mechanisms so far explored are specific to a particular scale or level of description of social dynamics. General mechanisms offering explanatory insights across different levels remain poorly articulated. The same problem applies to qualitative analyses trying to capture general principles of connected multitudes. These include perspectives stressing the individualistic logic pervading digital communication tools operating through sharing personalized content in social media [11], in sharp contrast

with narratives highlighting the powerful aggregating and unifying affordances of digital communication tools [12]. Reconciling these tensions, using the analogy of biological brains, we argue that what constitutes social collective ‘brains’ as complex entities cannot necessarily be captured by a single level of description but involves a capacity to display coordination at multiple scales [13], perhaps resembling neural large-scale synchronization over multiple frequency bands [14–16]. However, the principles operating behind networks of connected multitudes require further conceptual and experimental development to address gaps in extant theory.

Propitiously, the rise of social media and digital data-mining creates the opportunity for a novel analysis of human social systems [17] providing mechanisms for explaining their behaviour and opening-up the interactions between different scales of activity for detailed investigation. This opportunity provides an entry point into theoretical debates from where we can begin to generate hypothesis based on inferences from real world data. It is a position from which to undertake the difficult task of conceptualizing and describing the interwoven network of causal relations at different levels of description in social systems.

We use a data set of 1.5 million Twitter messages to explore transient phase-locking synchronization as a general mechanism explaining interactions within and between temporal scales. In particular, we use a well-known social event of large-scale social and political self-organization: the massive political protest of the 15M movement in Spain, emergent in the aftermath of the 2011 Arab Spring and widely thought to be facilitated through digital social platforms [18]. The exemplar of the 15M movement is interesting for a number of reasons: First, it consists in a self-organized social movement arising from online communication in a distributed network of citizens and civil associations (without significant coverage by mainstream media until days after the protests had taken to the streets). Second, the movement led to massive, nationwide demonstrations and encampments, creating a decentralized collective agency which has had a profound impact in Spanish politics [19–21]. Finally, a series of studies have characterized some of the emerging properties of the 15M and how it exhibits features typical of critical systems and distributed self-organization [22, 23].

Using this data set, we propose phase-locking statistics between geographical nodes at different frequencies as a generic description of coordination in a nationwide social system. This description allows us to use maximum entropy techniques to extract Ising models mapping the statistical mechanics of the system at each frequency band and thus obtain a deeper understanding of the spatiotemporal patterns of coordination within and between frequency bands. Inspecting the properties of the models at each frequency band we observe that all bands are operating near a critical point but that different frequencies play different roles in the system. While fast bands alternate states of (almost) full synchronization and full desynchronization, bands with slower frequencies display a wide range of possible configurations of metastable states with clusters of partial synchronization. Furthermore, applying transfer entropy in the energy landscape at each frequency described by the Ising models, we characterize cross-scale interactions showing an asymmetry between upward and downward influences, where high frequency synchronization influences nearby slower frequencies, while slow frequency bands are able to modulate distant faster bands. We argue that our results offer a promising step towards the description of general mechanisms operating at different scales, suggesting the existence of general rules for scaling up and down the dynamics of multitudinous collective systems.

Results

We use a data set of 1,444,051 time-stamped tweets from 181,146 users, collected through the Twitter streaming API between 13 May 2011 and 31 May 2011 [20] using T-Hoarder [24]. Messages were captured during 17 days during the Spanish 15M social unrest events in 2011 containing at least one of a set of 12 keywords or hashtags related to the protest (see reference [20] for a detailed description). We extracted geographical information from the location information of users (see SI Appendix), selecting the 15 urban areas with the largest number of messages. Using this information, we generated time-stamped series reflecting the number of tweets emitted from each city for intervals of 60 seconds.

Synchronization at multiple frequencies

One of the most prominent features of the 15M movement was its fast territorial development. Without any coordination centre or any formal organization, the movement was able to reproduce a network of camps across Spanish cities in a period of a few days. As this coordination between geographical nodes takes place at several temporal scales, we propose a generic description of these interactions based on the temporal coordination of oscillations at multiple frequencies. We analyse the coordination between populations at main Spanish cities using Morlet wavelet filtering to extract the phase content $\theta_i(f, t)$ of the activity time series at city i at time t and frequency f , with a span of frequencies in the range $[1.67 \cdot 10^{-3} \text{ Hz}, 9.26 \cdot 10^{-5} \text{ Hz}]$ (from 10 minutes to 3 hours) logarithmically distributed with intervals of $10^{0.01}$. We use phase-locking statistics [25] to define phase-locking values between two cities i and j as:

$$\phi_{ij}(f, t) = \left| \frac{1}{\delta} \sum_{\tau=-\delta/2}^{\delta/2} e^{i(\theta_y(f, t+\tau) - \theta_x(f, t+\tau))} \right| \cdot A_{ij}(t) \quad (1)$$

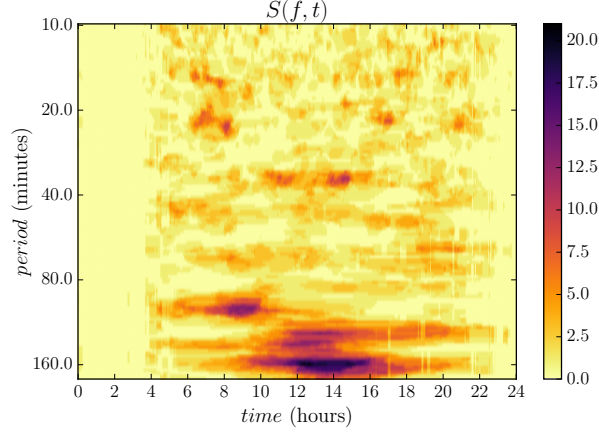


Figure 1. Phase-locking statistics. Sum of the number of phase-locking links between all cities $S(f, t)$ for day May 27. The horizontal axis represents a temporal span of instants t during the day, and the vertical axis represents the period corresponding to the frequency f of the wavelets used for extracting phase contents of the signals. The colour represents the sum of phase-locking links for f and t .

where δ is the size of the window of temporal integration: $\delta = \frac{n_c}{f}$, being n_c the number of cycles in which we analyse phase-locking. We use a value of $n_c = 8$ cycles, similar to the values typically used in neuroscience, ensuring that we are detecting sustained synchronization. $A_{ij}(t)$ is a corrector factor removing spurious synchronization when the network is inactive (e.g. during nighttime, see SI Appendix).

Statistical significance of phase-locking values is determined by comparing them to phase-locking values of surrogate time series obtained using the amplitude adjusted Fourier transform [26]. We use 200 surrogate time series to estimate a significance threshold for the values of $\phi_{ij}(f, t)$ for all values of f . The average phase-locking values of surrogate time series were used to compute a threshold $\phi_{th}(f)$, indicating a value higher than 99% of surrogate data. Using this threshold, we define phase-locking links between two cities i and j as statistically salient values of $\phi_{ij}(f, t)$:

$$\Phi_{ij}(f, t) = \begin{cases} 1, & \text{if } \phi_{ij}(f, t) \geq \phi_{th}(f) \\ 0, & \text{otherwise} \end{cases} \quad (2)$$

As we document in reference [27], using phase-locking statistics we find widespread moments of significant synchrony at different instants often corresponding with important moments of the 15M protests. For illustrative purposes, in Figure 1 we show the total number of phase-locking links $S(f, t) = \sum_{i,j} \Phi_{ij}(f, t)$ for a specific day of the protests. At faster frequencies (lower period) we observe short and less intense instants of synchrony, while at slower frequencies synchrony lasts for longer periods of time. Using wavelet pattern matching [28] over $S(f) = \langle S(f, t) \rangle$ after applying a linear detrending, we detect frequency peaks of synchronization in the system (see SI Appendix), identifying eight main frequency bands of synchronization f_k , $k = 1, \dots, 8$, where larger k corresponds to larger timescales (i.e. slower frequencies).

Pairwise maximum entropy modelling of phase-locking statistics

In order to inspect how these phase-locked coalitions are operating at each frequency band, we derive from our data statistical mechanics models of the system. With these models we can infer macroscopic properties from microscopic descriptions of the system. Using maximum entropy models we infer the probability distribution of possible states s of the network, corresponding to all the combinations of binary possibilities of each node being or not being phase-locked to other nodes in the network at a particular frequency of synchronization. For simplicity, we consider the state of a node i being phase-locked to a synchronized cluster, that is $s_i = 1$, when it has at least one synchronization link and (i.e. $\Phi_{ij} = 1$ for at least one value of j), and otherwise the state of the node is set to $s_i = -1$. We extract a pairwise maximum entropy model described by the Boltzmann distribution of an Ising model. This is the least-structured model that is consistent with the mean activation rate and correlations of the nodes in the network. Pairwise correlation maximum entropy models have been successfully used to map the activity of networks of neurons [29], antibody sequences [30] or flocks of birds [31]. These models, instead of being postulated as approximations of real phenomena, can infer exact mappings capturing measured properties of a system (means and correlations in our case), making them good candidates for capturing the structures underlying social coordination.

The maximum entropy distribution consistent with a known average energy is the Boltzmann distribution $P(s) = Z^{-1} e^{-\beta E(s)}$, where s is a state of the network, Z is the partition function and $\beta = \frac{1}{T k_B}$, being k_B Boltzmann's constant and T the temperature.

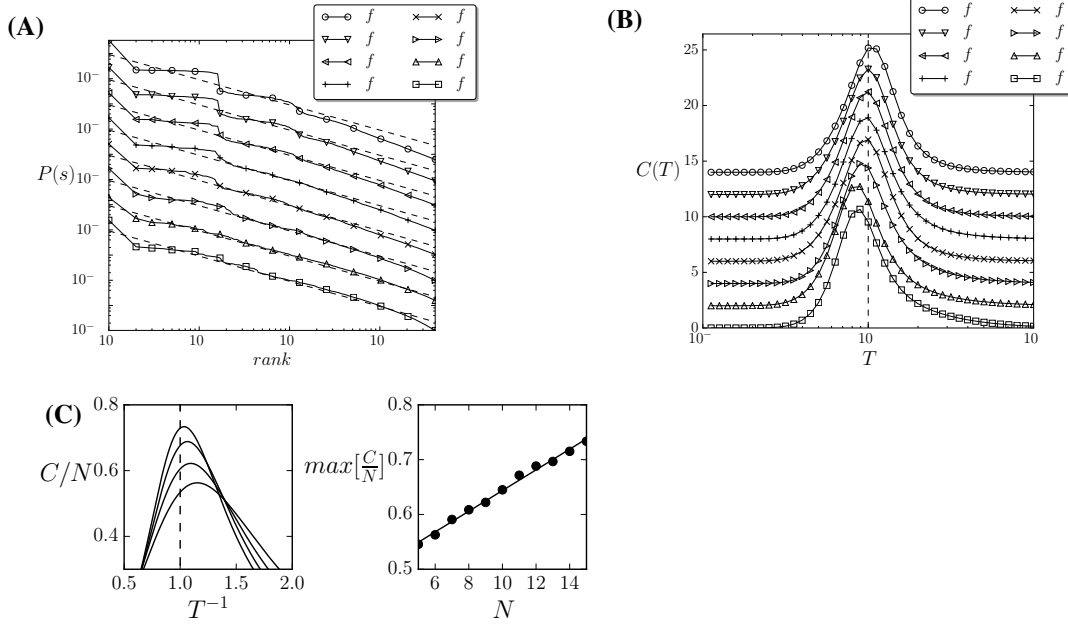


Figure 2. Signatures of criticality. (A) Ranked probability distribution function of the inferred Ising models for the different frequency bands (solid lines) versus a distribution following Zipf’s law, (i.e. $P(s) = 1/\text{rank}$, dashed lines). We observe a good agreement between the model and Zipf law, suggesting critical scaling. (B) Heat capacity versus temperature for the inferred Ising models for different frequency bands. Temperature $T = 1$ is the point where our models are poised, coinciding with a divergence of the heat capacity, which is a classical signature of criticality. In both graphs lines are shifted vertically in order to facilitate visualization of the distinct frequencies. (C) Divergence of the heat capacity with the syze of the system, showing the peaks of the normalized heat capacity of the Ising model at f_5 for sizes 6,9,12 and 15 (left) and linear trend of the normalized peak maxima for sizes 5 to 15 (right).

The energy of the model with pairwise interactions is defined as $E(s) = -\sum_i h_i s_i - \frac{1}{2} \sum_{i < j} J_{ij} s_i s_j$, where ‘magnetic fields’ h_i represent influences in the activation of individual nodes and ‘exchange couplings’ J_{ij} stand for the tendencies correlating the activity between nodes. Without loss of generality we can set the temperature $T = 1$. Considering a pairwise model, the resulting distribution of the maximum entropy model is:

$$P(s) = \frac{1}{Z} \exp \left[\beta \sum_i h_i s_i + \frac{1}{2} \sum_{i < j} J_{ij} s_i s_j \right] \quad (3)$$

where the h_i and J_{ij} are adjusted to reproduce the measured mean and correlation values between nodes in the network.

From the frequency bands f_k extracted in the previous section we extract models of pairwise correlations at the corresponding frequencies. For each frequency band, we infer an Ising model $P_{f_k}(s)$ solving the corresponding inverse Ising problem, using a coordinate descent algorithm (see Methods) for fitting the parameters h_i and J_{ij} that reproduce the means and correlations found in the series of states s for the description of phase-locking relations at each frequency.

The accuracy of the inferred models can be evaluated by testing how much of the correlation structure of the data is captured. One measure to evaluate this is the ratio of multi-information between model and real data [32]. In our case, our data limits us to computing the entropy of small sets of nodes (between 5 and 7, see SI Appendix). Limiting our entropy calculations to random sets of five to seven nodes, we can see in Figure S2 and Table S3 that our models are able to capture around 70% of the correlations in the data for subsets of the indicated sizes (see SI Appendix for a detailed description).

Once we have extracted a battery of models $P_{f_k}(s)$, indicating the probability distributions of phase-locking configurations at different frequency bands, we explore the thermodynamic (macroscopic) properties associated to them. First, we observe how all the models are poised at critical points. One signature of criticality we find is that the probability distribution of $P_{f_k}(s)$ follows a Zipf’s law (Figure 2.A), specially for slower values of f_k . Finding a scale-free distribution in our model is consistent with power laws appearing in the dynamics of the temporal series of tweet activity found in this data set [27] or in structural parameters in similar data sets [22]. Furthermore, the Ising models allow us to find further evidence of the critical

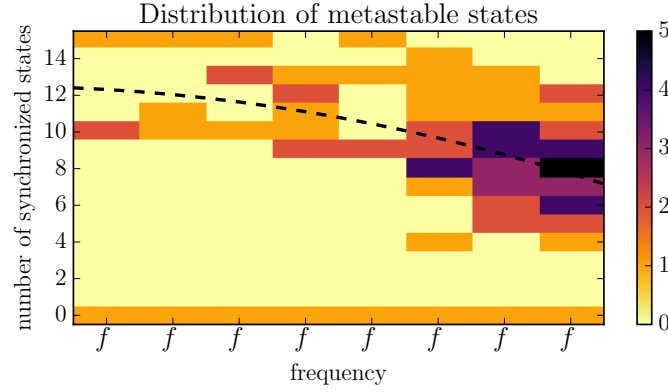


Figure 3. Distribution of metastable states by frequency and synchronized nodes. Distribution of the number of active (i.e. synchronized) states of the inferred Ising models for each frequency band. The horizontal axis represents the frequency band, the vertical axis the number of active states of the metastable states and the color represents the count of metastable states with the same number of active states. The dashed line is the result of a least squares second order polynomial fit (higher orders show a similar trend) over the number of active nodes of metastable states (excluding states with zero active nodes) with respect to the frequency index, showing a decrease of the number of synchronized nodes in the metastable states in favour of local clusters of activity.

behaviour of the model by exploring divergences in their heat capacity. By introducing a fictitious temperature value changing the temperature parameter T (previously assumed to be equal to 1), we compute the heat capacity of the system as:

$$C(T) = T \frac{\partial H[P(s)]}{\partial T} = \frac{1}{T^2} \langle E^2(s) \rangle - \langle E(s) \rangle^2 \quad (4)$$

where $H[P(s)]$ is the Shannon Entropy of the probability distribution of an Ising model. A divergence in the heat capacity of the system is an indicator of critical phenomena. As we observe in Figure 2.B, for all f_k the peak of the heat capacity is around the value $T = 1$ suggesting that the models are poised just at critical points. Inferring the Ising models to match subsets of the network nodes (see SI Appendix), we observe how the normalized peak in the heat capacity diverges with the system size (the specific – although representative – case of f_5 is shown in Figure 2.C), where $C(T)/N$ grows with N with a linear rate in the range $[0.012, 0.021]$ (see SI Appendix). Together with the Zipf distribution, the divergence of the heat capacity strongly suggests that social coordination phenomena in the 15M social network are operating in a state of criticality [32].

The fact that all frequency bands are operating near critical points does not mean that they are displaying the same behaviour. We can extract more information about the behaviour of the system at each frequency by analysing the presence of locally-stable or metastable states in the system. Metastable states are defined as states whose energy is lower than any of its adjacent states, where adjacency is defined by single spin flips. This means that in a deterministic state (i.e. a Hopfield network with $T = 0$) these points would act as attractors of the system. In our statistical model metastable states are points in which the system tends to be poised, since their probability is higher than any of its adjacent states. Finding the metastable states of the models at each frequency, we observe how the number of metastable states increases for slower frequencies (Figure S4.B), as the model presents a higher number of negative (inhibitory) couplings J_{ij} (see Figure S4.A).

Moreover, if we count the number of nodes that are phase-locked (i.e. the sum of all nodes with $s_i = 1$) for each metastable state represented in Figure 3, we observe important distinctions among frequency bands. For faster values of f_k there are only a few metastable states: a state where all nodes are not phase-locked (i.e. the system is completely desynchronized), and a few values where almost all nodes are phase-locked. Thus, at fast frequencies synchronization rapidly spreads from zero to all nodes in the network. On the other hand, for slower frequencies the number of metastable states grows and the number of phase-locked nodes for each state decreases. This shows that slow frequency synchronizations allows the creation of a variety of clusters of partial synchronization, allowing parts of the network to sustain a differentiated behaviour.

These results suggests that fast and slow synchronization frequencies in the network operate in complementary regimes –all operating near critical points– the former rapidly propagating information to all the network and the latter sustaining a variety of configurations responding to specific situations. Systems in critical points present a wide range of dynamic scales of activity and maximal sensitivity to external fluctuations. These features may be crucial for large systems that are self-organized in a distributed fashion. The presence of these complementary modes of critical behaviour at different frequency bands suggests

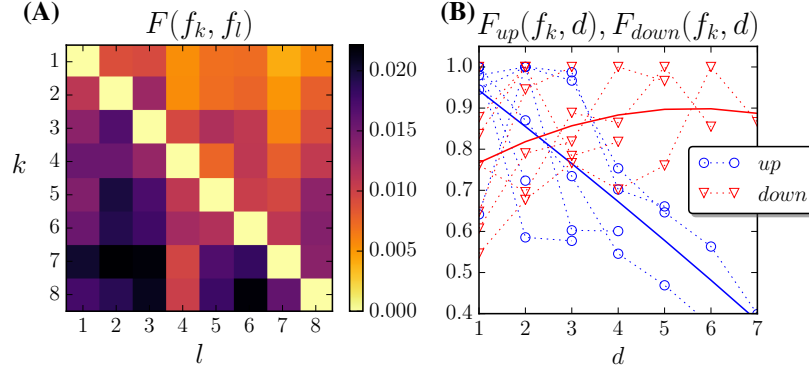


Figure 4. Average transfer entropy. (A) Average transfer entropy $F(f_k, f_l)$ across values of τ between energy levels at different frequencies. (B) Tendencies of upward ($F_{up}(f_k, d)$, blue circle markers) and downward ($F_{down}(f_k, d)$, red triangular markers) transfer entropy values respect to the distance d between frequencies. Solid lines represent a least squares second order polynomial fit (higher orders show a similar trend) of the values of $F_{up}(f_k, d)$ (blue solid line) and $F_{down}(f_k, d)$ (red solid line) respect to d . We observe how upward transfer entropy values display an important decrease with distance, whereas upward transfer entropy presents slightly larger values for larger distances.

that the system might be operating in a state of self-organized criticality, in which frequency bands adaptively regulate each other in order to maintain a global critical behaviour.

Cross-scale interactions in synchronization dynamics

Modelling phase-locking statistics provides a characterization of the interactions within frequency bands of synchronization. Furthermore, differences in the metastable states at each frequency band suggest what kind of interactions take place between distinct temporal scales. Because our definition of phase-locking statistics is restricted to interactions within the same frequency, we cannot use the computed phase-locking statistics to directly model inter-scale phase-locking between different frequencies (e.g. 2:1 phase-locking). However, we can use the thermodynamic descriptions of the system provided by maximum entropy models to simplify the analysis of inter-scale relations in real data.

Analysis of multiscale causal relations is typically a difficult task, and in our case we have to deal with a system of a high number of dimensions ($15 \cdot 8 = 120$ dimensions). Nevertheless, the Ising models describe the stability of the configurations of the 15 nodes in the network at each frequency band with an energy value. Thus, an easier way to describe multiscale interactions is to observe how fluctuations in the energy at one level affect the energy of the system at other levels, reducing the dimensions we have to deal with to only the 8 frequencies of synchronization.

We characterize the information flow between frequency bands using transfer entropy [33] between energy levels at each frequency $E_{f_k}(s)$. Transfer entropy captures the decrease of uncertainty in the state of a variable Y derived from the past state of other variable X :

$$\mathcal{T}_{X \rightarrow Y}(\tau) = \sum_{x_{t+\tau}, x_t, y_t} P(x_{t+\tau}, x_t, y_t) \log \frac{P(x_{t+\tau} | x_t, y_t)}{P(x_{t+\tau} | x_t)} \quad (5)$$

where x_t denotes the state of X at time t and τ indicates the temporal distance used to capture interactions.

In order to compute transfer entropy over energy values between timescales, we discretize the values of energy $E_{f_k}(s)$ into a variable with 3 discrete bins $E_{f_k}^*(s)$ using the Jenks-Caspall algorithm [34]. The value of 3 bins was selected to optimize the computation of joint probability density functions (see SI Appendix) although we tested values from 2 to 6 bins with similar results. Using transfer entropy we estimate the causal interactions between energetic states at each timescale by computing the values of $\mathcal{T}_{E_{f_k}^* \rightarrow E_{f_l}^*}(\tau)$ (see the SI Appendix for a representation of transfer entropy functions) for values of τ between 1 and 2^9 minutes (i.e. up to 8.5 hours) logarithmically distributed with intervals of $2^{0.25}$.

To simplify the interpretation of the data, we compute the average value of transfer entropy (across the logarithmic range of τ) for pairs of frequencies as $F(f_k, f_l) = \langle \mathcal{T}_{E_{f_k}^* \rightarrow E_{f_l}^*}(\tau) \rangle$ (Figure 4.A). Moreover, we separate the values of upward and downward flows of information for each node, characterizing $F_{up}(f_k, d) = F(f_{k-d}, f_k) / \max_d[F(f_{k-d}, f_k)]$ and $F_{down}(f_k, d) = F(f_{k+d}, f_k) / \max_d[F(f_{k+d}, f_k)]$, where d takes values between 1 and 7, and upward and downward entropies are divided by their maximum values in order to compare transfer entropy between nodes with distinct values of entropy. In Figure 4.B, we

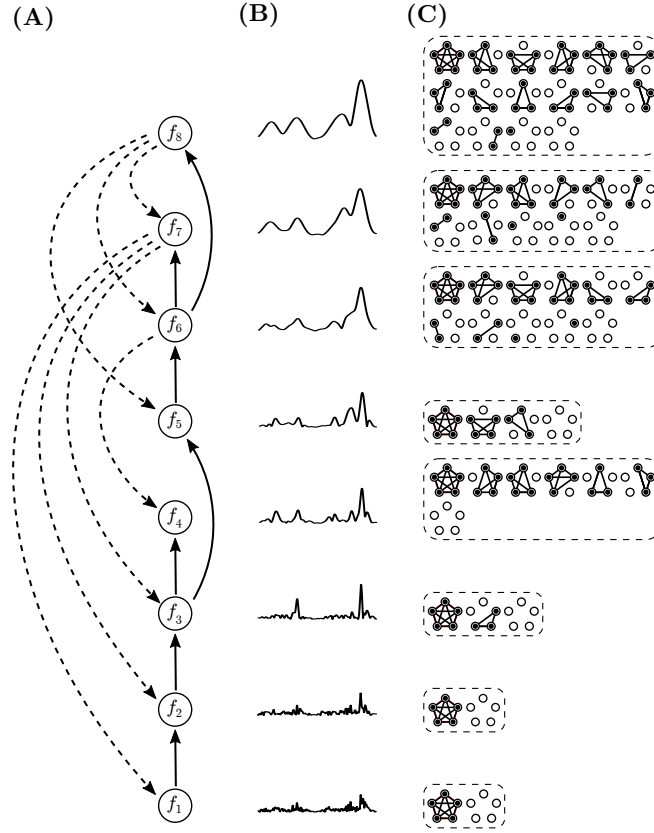


Figure 5. Cross-scale interactions in social coordination. Schematic displaying the results presented in previous figures. (A) Interactions in terms of average transfer entropy between energy levels at different frequencies described by $F_{up}(f_k, d)$ and $F_{down}(f_k, d)$. For simplicity only the largest upward (solid arrows) and downward (dashed arrows) transfer entropy values are represented. (B) Fragment of activity of all nodes in the network (in number of tweets per second) filtered by the different wavelets used in the filtering of frequency bands. (C) Metastable states of the models at each frequency. For simplicity, only metastable configurations of the five cities with largest total volume of activity are represented.

observe upward and downward flows of information. As we can see, upward flows decrease importantly with distance between scales. In contrast, downward flows increase slightly with distance between scales.

These results show an interesting picture of cross-scale interactions. While in upward interactions energy at each frequency band only influences neighbouring slower bands, in downward interactions slow frequency bands modulate distant faster bands. We also observe this in the schematic in Figure 5.A, where for simplicity only the largest values of $F_{down}(f_k, d)$ and $F_{down}(f_k, d)$ are displayed for each frequency band. These results suggest that there might be general rules for scaling up and scaling down social coordination dynamics in a nested structure of frequency bands. The mechanisms involved might resemble those found in neuroscience, where upward cascades have been found to take place in the form of avalanches propagating local synchrony and downward cascades take the form of phase-amplitude modulation of local high-frequency oscillations by large-scale slow oscillations [16]. Future research is required for testing the application of these rules to other social coordination phenomena and the specific mechanisms operating behind upward and downward cross-scale interactions.

Discussion

It is appealing to think that general coordinative mechanisms may be suited to explain the behaviour of social systems at different scales. Here, using a large-scale social media data set, we have shown how the application of maximum entropy inference methods over phase-locking statistics at different frequencies offers the prospect of understanding collective phenomena at a deeper level. The presented results provide interesting insights about the self-organization of digitally connected multitudes. Our contribution shows that phase-locking mechanisms at different frequencies operate in a state of criticality for rapidly integrating the activity of the network at fast frequencies while building-up an increasing diversity of distinct configurations

at slower frequencies. Moreover, the asymmetry between upward and downward flows of information suggests how social systems operating through distributed transient synchronization may create a hierarchical structure of temporal timescales, in which hierarchy is not reflected in a centralized control but in the asymmetry of information flows between the coordinative structures at different frequencies of activity. This offers a tentative explanation of how an unified collective agency, such as the 15M movement in Spain, might emerge in a distributed manner from mechanisms of transient large-scale synchronization. Of particular interest would be to test the extent our findings about the structural and functional relations of social coordination apply to other self-organizing social systems, or their relation with mechanisms of cross-scale interactions known from large-scale systems neuroscience. A new generation of experimental findings based on statistical mechanics models may provide the opportunity to discover the mechanisms behind multitudinous social self-organization.

Methods

Data availability

The data employed in this study was kindly provided by the authors of reference [20].

Learning pairwise maximum entropy models from data

Ising models are inferred using an adapted version of the coordinate descent algorithm described in reference [35]. The coordinate descent algorithm works by iteratively adjusting a single weight h_i or J_{ij} that will maximize an approximation of the change in the empirical logarithmic loss between the observed data and the model, computed through the means and correlations present in the empirical data and the model. The code implementing the coordinate descent algorithm is available at <https://github.com/MiguelAguilera/ising>.

References

1. W. H. McNeill, *Keeping Together in Time: Dance and Drill in Human History*. New York, USA: ACLS Humanities E-Book, Aug. 2008.
2. K. Hill, “Anabaptism and the World of Printing in Sixteenth-Century Germany,” *Past & Present*, vol. 226, pp. 79–114, Feb. 2015.
3. D. Chang, Y. Ge, S. Song, N. Coleman, J. Christensen, and J. Heer, “Visualizing the Republic of Letters,” *Stanford: Stanford University*. Retrieved April, vol. 21, p. 2014, 2009.
4. M. Castells, “Communication, Power and Counter-power in the Network Society,” *International Journal of Communication*, vol. 1, p. 29, Feb. 2007.
5. P. Levy, *Collective Intelligence: Mankind’s Emerging World in Cyberspace*. Perseus Books, 1999.
6. H. Rheingold, *Smart Mobs: The Next Social Revolution*. Basic Books, Mar. 2007.
7. W. L. Bennett, A. Segerberg, and S. Walker, “Organization in the crowd: peer production in large-scale networked protests,” *Information, Communication & Society*, vol. 17, pp. 232–260, Feb. 2014.
8. E. Ferrara, O. Varol, F. Menczer, and A. Flammini, “Traveling trends: social butterflies or frequent fliers?,” in *Proceedings of the first ACM conference on Online social networks*, pp. 213–222, 2013.
9. M. Oka, Y. Hashimoto, and T. Ikegami, “Self-Organization on Social Media: Endo-Exo Bursts and Baseline Fluctuations,” *PLoS ONE*, vol. 9, p. e109293, Oct. 2014.
10. O. Varol, E. Ferrara, C. L. Ogan, F. Menczer, and A. Flammini, “Evolution of Online User Behavior During a Social Upheaval,” in *Proceedings of the 2014 ACM Conference on Web Science*, WebSci ’14, pp. 81–90, 2014.
11. W. L. Bennett and A. Segerberg, “The logic of connective action: Digital media and the personalization of contentious politics,” *Information, Communication & Society*, vol. 15, no. 5, pp. 739–768, 2012.
12. J. S. Juris, “Reflections on #Occupy Everywhere: Social media, public space, and emerging logics of aggregation,” *American Ethnologist*, vol. 39, pp. 259–279, May 2012.
13. A. Monterde, A. Calleja-López, M. Aguilera, X. E. Barandiaran, and J. Postill, “Multitudinous identities: a qualitative and network analysis of the 15m collective identity,” *Information, Communication & Society*, vol. 18, pp. 930–950, Aug. 2015.
14. F. Varela, J.-P. Lachaux, E. Rodriguez, and J. Martinerie, “The brainweb: Phase synchronization and large-scale integration,” *Nature Reviews Neuroscience*, vol. 2, pp. 229–239, Apr. 2001.
15. G. Buzsaki, *Rhythms of the Brain*. Oxford University Press, Aug. 2006.

16. M. Le Van Quyen, "The brainweb of cross-scale interactions," *New Ideas in Psychology*, vol. 29, pp. 57–63, Aug. 2011.
17. D. Lazer, A. Pentland, L. Adamic, S. Aral, A.-L. Barabási, D. Brewer, N. Christakis, N. Contractor, J. Fowler, M. Gutmann, T. Jebara, G. King, M. Macy, D. Roy, and M. V. Alstyne, "Computational Social," *Science*, vol. 323, pp. 721–723, Feb. 2009.
18. J. Postill, "Digital politics and political engagement," *Digital Anthropology*, pp. 165–184, 2013.
19. V. Sampedro and J. Lobera, "The Spanish 15-M Movement: a consensual dissent?," *Journal of Spanish Cultural Studies*, vol. 15, pp. 61–80, Apr. 2014.
20. I. Peña-López, M. Congosto, and P. Aragón, "Spanish Indignados and the evolution of the 15m movement on Twitter: towards networked para-institutions," *Journal of Spanish Cultural Studies*, vol. 15, pp. 189–216, Apr. 2014.
21. S. Tormey and R. A. Feenstra, "Reinventing the political party in Spain: the case of 15m and the Spanish mobilisations," *Policy Studies*, vol. 36, pp. 590–606, Nov. 2015.
22. J. Borge-Holthoefer, A. Rivero, I. García, E. Cauhé, A. Ferrer, D. Ferrer, D. Francos, D. Iñiguez, M. P. Pérez, G. Ruiz, F. Sanz, F. Serrano, C. Viñas, A. Tarancón, and Y. Moreno, "Structural and Dynamical Patterns on Online Social Networks: The Spanish May 15th Movement as a Case Study," *PLoS ONE*, vol. 6, p. e23883, Aug. 2011.
23. J. Borge-Holthoefer, N. Perra, B. Gonçalves, S. González-Bailón, A. Arenas, Y. Moreno, and A. Vespignani, "The dynamics of information-driven coordination phenomena: A transfer entropy analysis," *Science Advances*, vol. 2, Apr. 2016.
24. M. Congosto, P. Basanta-Val, and L. Sanchez-Fernandez, "T-Hoarder: A framework to process Twitter data streams," *Journal of Network and Computer Applications*, vol. 83, pp. 28–39, Apr. 2017.
25. J.-P. Lachaux, E. Rodriguez, M. Le Van Quyen, A. Lutz, J. Martinerie, and F. J. Varela, "Studying single-trials of phase synchronous activity in the brain," *International Journal of Bifurcation and Chaos*, vol. 10, no. 10, pp. 2429–2439, 2000.
26. T. Schreiber and A. Schmitz, "Improved Surrogate Data for Nonlinearity Tests," *Physical Review Letters*, vol. 77, pp. 635–638, July 1996.
27. M. Aguilera, "The Collective Mind: large-scale self-organization in social systems," in *Interaction dynamics and autonomy in cognitive systems*, pp. 211–248, Universidad de Zaragoza, 2015.
28. P. Du, W. A. Kibbe, and S. M. Lin, "Improved peak detection in mass spectrum by incorporating continuous wavelet transform-based pattern matching," *Bioinformatics*, vol. 22, pp. 2059–2065, Sept. 2006.
29. E. Schneidman, M. J. Berry, R. Segev, and W. Bialek, "Weak pairwise correlations imply strongly correlated network states in a neural population," *Nature*, vol. 440, pp. 1007–1012, Apr. 2006.
30. T. Mora, A. M. Walczak, W. Bialek, and C. G. Callan, "Maximum entropy models for antibody diversity," *Proceedings of the National Academy of Sciences*, vol. 107, pp. 5405–5410, Mar. 2010.
31. W. Bialek, A. Cavagna, I. Giardina, T. Mora, E. Silvestri, M. Viale, and A. M. Walczak, "Statistical mechanics for natural flocks of birds," *Proceedings of the National Academy of Sciences*, vol. 109, pp. 4786–4791, Mar. 2012.
32. T. Mora and W. Bialek, "Are biological systems poised at criticality?," *Journal of Statistical Physics*, vol. 144, no. 2, pp. 268–302, 2011.
33. T. Schreiber, "Measuring Information Transfer," *Physical Review Letters*, vol. 85, pp. 461–464, July 2000.
34. G. F. Jenks and F. C. Caspall, "Error on Choroplethic Maps: Definition, Measurement, Reduction," *Annals of the Association of American Geographers*, vol. 61, pp. 217–244, June 1971.
35. M. Dudík, S. J. Phillips, and R. E. Schapire, "Performance Guarantees for Regularized Maximum Entropy Density Estimation," in *Learning Theory* (J. Shawe-Taylor and Y. Singer, eds.), no. 3120 in Lecture Notes in Computer Science, pp. 472–486, Springer Berlin Heidelberg, July 2004.

Acknowledgements

Research was supported in part by the Spanish National Programme for Fostering Excellence in Scientific and Technical Research project PSI2014-62092-EXP and project TIN2016-80347-R funded by the Spanish Ministry of Economy and Competitiveness.

Supplementary Information

Data preprocessing

We use a data set of 1,444,051 tweets from 181,146 users, collected between 13 May 2011 and 31 May 2011. This data set was extracted from the Twitter streaming API, which provides information on the time and content of the tweet, as well as information on the sender, including location. Messages were captured when they contained one of the following hashtags or keywords (which were selected as some of the most relevant during the emergence of the 15M movement): #15M, 15-M, #democraciarealya, #tomalacalle, #Nolesvotes, #spanishrevolution, #acampadasol, #acampadabcn, #indignados, #notenemosmiedo, #nonosvamos, #yeswecamp. We filter messages in the data set using the location field in the description of the user that sent the message. Since the 15M was (at least during the first days) mainly an urban phenomena, we analyse geographical interactions between the 15 cities with more activity in Twitter during 17 days of the protests. We find the 15 names of cities most repeated in the data set, and counted messages corresponding to a specific city when the city name appeared in the location field. Since the location is a field of the description of the user, it does not necessarily correspond to the real location of the user at the moment the message was sent. We ran a test on geolocalized Twitter data from Spain, observing that for a set of 20.000 random tweets in a 80.25% the profile location corresponds with the actual geolocation of the user, giving the information of the user's location field a moderately high reliability.

Phase-locking statistics

Time series of activity at each city are generated by counting the number of messages from users located at the city in intervals of 60 seconds for a period comprising 17 days, starting at 2AM May 14th 2011. Each time series is filtered using Morlet wavelets at different frequencies. For each city i and frequency f we extract the phase content $\theta_i(f, t)$ for each moment of time t , with a frequency span between $[1.67 \cdot 10^{-3} \text{Hz}, 9.26 \cdot 10^{-5} \text{Hz}]$ (from 10 minutes to 3 hours) mapped into a logarithmic sequence with intervals of $10^{0.01}$.

Phase-locking values are defined for each pair of cities i and j as defined in Equation 1. We introduce a corrector factor $A_{ij}(t)$ to remove spurious synchronization when the network is inactive. $A_{ij}(t)$ is zero when the mean activity of node i or node j for a moving window of 30 minutes is below a threshold of 0.25 times its mean activation, which generally happened during some periods at night.

From phase-locking values we extract phase-locking links, which are activated when the phase-locking value is higher than 99% of a set of 200 surrogate time series we generate for purposes of statistical validation, as indicated in Equation 2. Surrogate time series are generated using amplitude adjusted Fourier transform using the TISEAN software (Available at http://www.mpipks-dresden.mpg.de/~tisean/Tisean_3.0.1/). Amplitude adjusted Fourier transform surrogates are time series that preserve the power spectrum of a distribution and a distribution of values, but remove the temporal correlations present in the original signal.

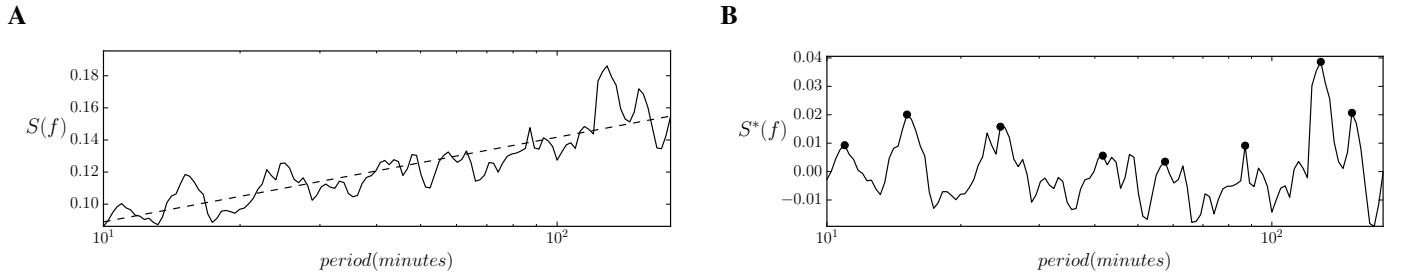


Figure S1. Peaks of salient synchronization. (A) Sum of total phase locking links $S(f)$ for each value of frequency (solid line). We detect a log-linear trend that we remove for detecting synchronization peaks. (B) Detrended $S(f)$ for each value of frequency (solid line). Synchronization peaks found using a two-dimensional wavelet transform (black dots).

Detection of salient synchronization frequency bands

We localize frequency bands synchronization by detecting peaks of salient phase-locking links in the logarithmic frequency space. We compute the mean number of synchronization links for each frequency as the temporal mean of phase locking links at that frequency $S(f) = \langle \sum_{i,j} \Phi_{ij}(f, t) \rangle$ (Figure S1.A). As $S(f)$ increases with slower frequencies following approximately a log-linear trend, we approximate the trend computing a least squares first order polynomial fit respect to the logarithm of f and remove it from $S(f)$ obtaining a detrended function. $S(f)^*$ In order to robustly detect peaks, we apply a two-dimensional wavelet transform of the detrended $S(f)$ over the vector of logarithmic frequencies. Using 10 Ricker wavelets

Label	Frequency
f_1	$1.52e-3Hz$
f_2	$1.10e-3Hz$
f_3	$6.78e-4Hz$
f_4	$4.00e-4Hz$
f_5	$2.90e-4Hz$
f_6	$1.91e-4Hz$
f_7	$1.29e-4Hz$
f_8	$1.10e-4Hz$

Table S1. Frequencies of salient synchronization. Table representing the frequency values corresponding to the peaks represented in Figure S1.B.

Label	Number of transitions between states
f_1	2276
f_2	1903
f_3	1387
f_4	922
f_5	865
f_6	692
f_7	731
f_8	641

Table S2. Number of state transitions for each frequency. Number of transitions between states s from the data used for computing the Ising model at each selected frequency.

of widths from 1 to 10 steps in the selected logarithmic range of frequency (i.e. a range of $[1.67 \cdot 10^{-3}Hz, 9.26 \cdot 10^{-5}Hz]$ logarithmically distributed with intervals of $10^{0.01}$) we compute the wavelet transform matrix and detect its ridge lines to find eight peaks of salient synchronization (code available at https://github.com/scipy/scipy/blob/v0.14.0/scipy/signal/_peak_finding.py#L410). As the position of the detected peaks vary slightly depending on the parameters employed, we adjust the position of each peaks by climbing to the nearest local maxima if one is found within a distance of two steps. In Figure S1.B we observe the result of the process and the 8 detected peaks. From these peaks we extract 8 frequencies f_k , with $k = 1, \dots, 8$, indicating the position of the peaks in $S(f)$ (Table S1).

Number of samples required to compute probability distributions

When we compute multi-informations and transfer entropies from the data set, we face a compromise between the size of the probability distribution function of the system (corresponding to 2^N states) and the number of samples we employ for calculating it. In order to correctly compute these probability distributions, we need to ensure that the number of samples found in our data is sufficiently large for describing the frequency of occurrence of all possible states. Although the number of samples in our data is large, as data changes at different frequencies, slower frequencies may present a smaller number of transitions between states than fast frequencies, therefore offering a reduced effective sample of visited states.

In order to quantify the number of states visited at each frequency, we count the number of transitions between states s used to infer the Ising models at each frequency (Table S2). Knowing that number, we can estimate a threshold of how many states can have a probability distribution to be accurately estimated from our samples at different frequencies. We arbitrarily establish a requirement of the number of transitions being larger than 2^4 times the number of possible states of the objective probability distribution function. Although the exact value of the threshold is arbitrary, during the analysis we tried different thresholds to ensure the robustness of the results.

Multi-information measures for assessing the accuracy of maximum entropy models

Once we infer the maximum entropy models that correspond to the means and correlations found in phase-locking data, it is important to characterize what is the accuracy of the model, that is, to what extent the statistical model generated is mapping the data we used in the inference. The accuracy of the model can be further evaluated by asking how much of the correlative structure found in the data is captured. We can measure the overall strength of correlations in the network using multi-information, which is defined as the total reduction in entropy relative to an independent model $I = H[P_1] - H[P_r]$, where

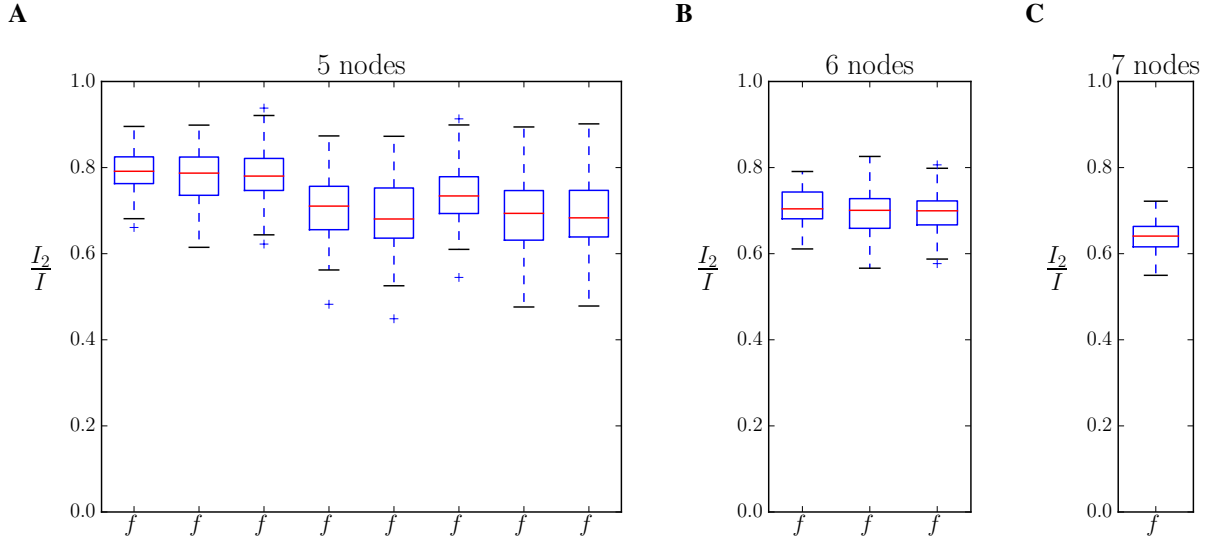


Figure S2. Accuracy of the model. Values of $\frac{I_2}{I}$ for subsets of combinations of nodes at each frequency. Each boxplot represents the distribution of $\frac{I_2}{I}$ for 100 subsets of n nodes at a specific frequency band selected randomly comparing the multi-information of the model and real data.

$H[P_r]$ is the entropy of the distribution of the real system whose data we are analysing and $H[P_1]$ is the entropy of an independent model. In our case, an independent model would be the equivalent of adjusting an Ising model in which the couplings are zero, and thus its energy function is defined as $E(s) = -\sum_i h_i s_i$. Multi-information can as well be used to compute the reduction of entropy of the distributions P_2 of the pairwise Ising model we inferred from data as $I_2 = H[P_1] - H[P_2]$. The ratio between these two quantities gives the fraction of the correlations captured by the pairwise Ising model:

$$\frac{I_2}{I} = \frac{H[P_1] - H[P_2]}{H[P_1] - H[P_r]} \quad (1)$$

Unfortunately, the data available is not enough for reliably computing P_r . The probability distribution P_r has a number of possible states of 2^{15} , while in our data the number of different states transited by the system is one or two orders of magnitude inferior, depending on the frequency. However, we can compute accurately subsets of the complete probability distribution $P_r(s'_i)$, with $\{s'_i\} \subset \{s_i\}$. For each frequency, we count the number of transitions between states found in the time series in our data, and contrast that number with the dimension of the subset of the probability function using a number n of nodes, i.e. 2^n . We use an arbitrary threshold requiring the number of states being at least 2^4 times larger than the number of values of the probability distribution function. Different thresholds yield slightly different results, although they don't change significantly the final results. We find that for frequencies from f_4 to f_8 we can compute reliably subsets with up to 5 nodes. For frequencies f_2 and f_3 the number increases to up to 6 and for f_7 it is 7 nodes.

In Figure S2 we can observe the distribution of the values of $\frac{I_2}{I}$ for 100 random choices of subsets for each number of nodes. We can observe that most of the subsets the values of $\frac{I_2}{I}$ indicate that between 60% and 80% of the correlations are captured (Table S3)

The limited availability of data, specially for slower frequencies, prevents us to compute the accuracy of the model for subsets with larger number of nodes. Future analysis applied to larger data sets should test if the accuracy of the model holds for capturing the correlations between larger subsets of nodes.

Parameters of the Ising models

Here we display the parameters h and J inferred for the Ising models at each frequency. As we observe in Figure S5, as we move from faster to slower frequencies, the amplitude of h and J increases. As well, the percentage of negative couplings increases. We compute the ratio of negative couplings as:

$$r_{neg} = \frac{0.5 \sum_{i < j} (J_{ij} - |J_{ij}|)}{\sum_{i < j} |J_{ij}|} \quad (2)$$

Frequency	$n = 5$	$n = 6$	$n = 7$
f_1	$\mu = 0.790, \sigma = 0.0493$	$\mu = 0.707, \sigma = 0.0434$	$\mu = 0.696, \sigma = 0.0341$
f_2	$\mu = 0.778, \sigma = 0.0596$	$\mu = 0.696, \sigma = 0.0520$	
f_3	$\mu = 0.782, \sigma = 0.0602$	$\mu = 0.698, \sigma = 0.0497$	
f_4	$\mu = 0.707, \sigma = 0.0748$		
f_5	$\mu = 0.692, \sigma = 0.0832$		
f_6	$\mu = 0.739, \sigma = 0.0693$		
f_7	$\mu = 0.685, \sigma = 0.0863$		
f_8	$\mu = 0.687, \sigma = 0.0928$		

Table S3. Distributions of multi-information ratios. Mean and standard deviation for each distribution in Figure S2.

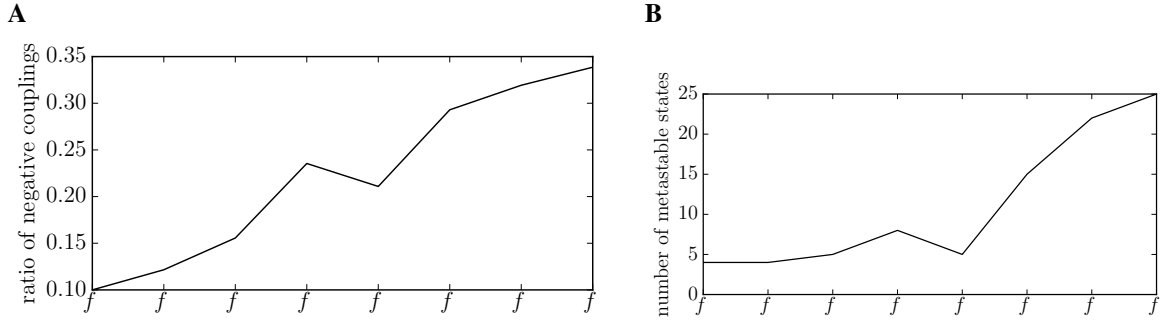


Figure S3. Negative couplings and number of metastable states. (A) Ratio of negative couplings for the inferred values of J_{ij} for each frequency. (B) Count of the number of metastable states for each frequency.

In figure S3.A we can observe how the ratio of negative coupling increases with slower frequencies. It is known from spin glass theory that metastable states emerge when some of the couplings between variables are negative. In Figure S3 we can observe how there is a correlation between the ratio of negative couplings and the number of metastable states.

Divergence of the heat capacity

At critical points, derivatives of thermodynamic quantities of the system as the entropy may diverge. An example of this is the heat capacity, whose divergence is a sufficient condition for criticality (though not a necessary one). To test the divergence of the heat capacity of the system, we extract Ising models of different sizes related to each frequency f_k . From sizes 5 to 15, we extract models inferring the set of means and correlation from the first N nodes of the system in order of increasing number of tweets emitted. For each model, we compute the normalized heat capacity $C(T)/N$. In Figure S4.A we observe the divergence of the maximum value of the peaks for sizes $N = 6, 9, 12, 15$. As size increases, the peak is higher and closer to $T = 1$. In Figure S4.B we represent the linear trend of the peaks from size 5 to 15. Trends are computed using a least squares first order polynomial fit. We identify trends with slopes in the range $[0.012, 0.021]$. A linear trend of $\max[C(T)/N]$ corresponds to a quadratic increment in the peak of the heat capacity $C(T)$ as N increases, suggesting a divergence of the heat capacity of the system.

Transfer entropy

Using the energy of the Ising models E_{f_k} at different frequencies, we compute transfer entropy by discretizing energy functions into clustered variables $E_{f_k}^*$. We apply natural Break classification through the Jenks-Caspall algorithm (code available at <https://github.com/domlysz/Jenks-Caspall.py>), which for each cluster minimizes the average deviation from the cluster's mean to determine the best arrangement of values into different clusters. Since computing transfer entropies requires to compute joint probability functions with three variables, to meet the same criteria we used to compute multi-information, we use a number of 3 clusters to ensure that for all the frequencies we have a number of samples of transited states which is at least 2^4 times larger than the values in the probability distribution. After discretizing the energy functions we compute the values of transfer entropies $\mathcal{T}_{kl}(\tau) = \mathcal{T}_{E_{f_k}^* \rightarrow E_{f_l}^*}(\tau)$ for values of τ in a range between $[1, 2^8]$ (i.e. from 1 minute to more than 4 hours) logarithmically distributed with intervals of $2^{0.25}$. Functions $\mathcal{T}_{kl}(\tau) = \mathcal{T}_{E_{f_k}^* \rightarrow E_{f_l}^*}(\tau)$ for different values of k and l are represented in Figure S6

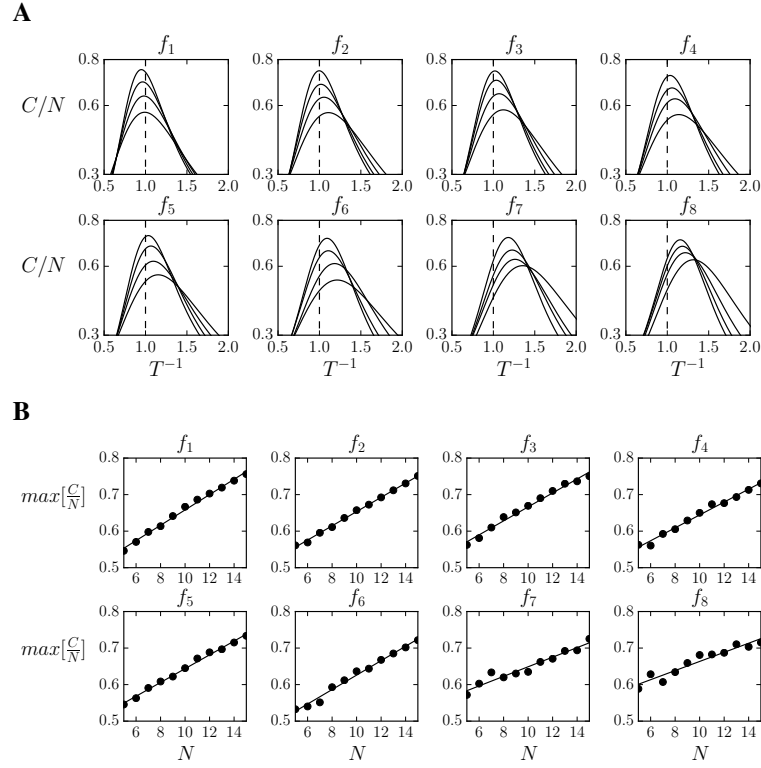


Figure S4. Divergence of the heat capacity of the system. (A) Normalized heat capacity $C(T)/N$ of the Ising models for sizes 6, 9, 12 and 15, where the larger peaks corresponds to larger sizes. (B) Linear trend (solid line) of the peaks of $C(T)/N$ (dots) respect the size of the system.

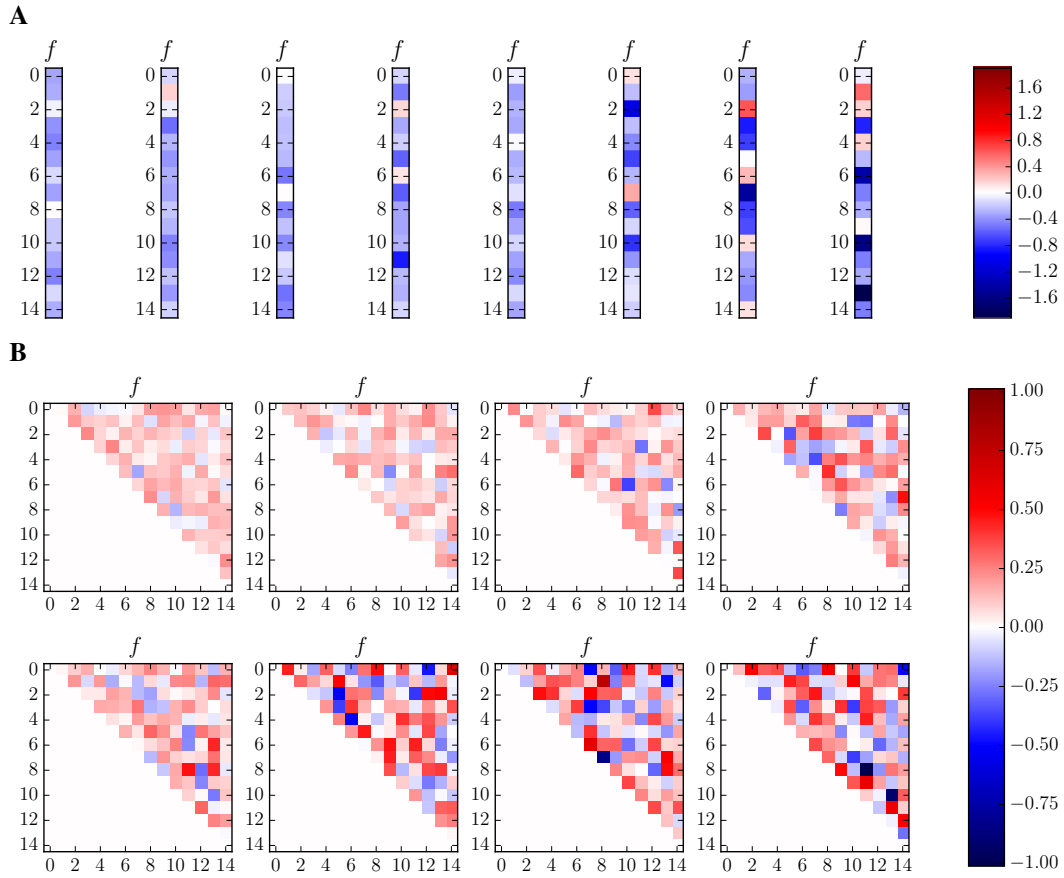


Figure S5. Parameters of the Ising models. For each frequency, we depict the parameters h (A) and J (B) of the inferred Ising models.

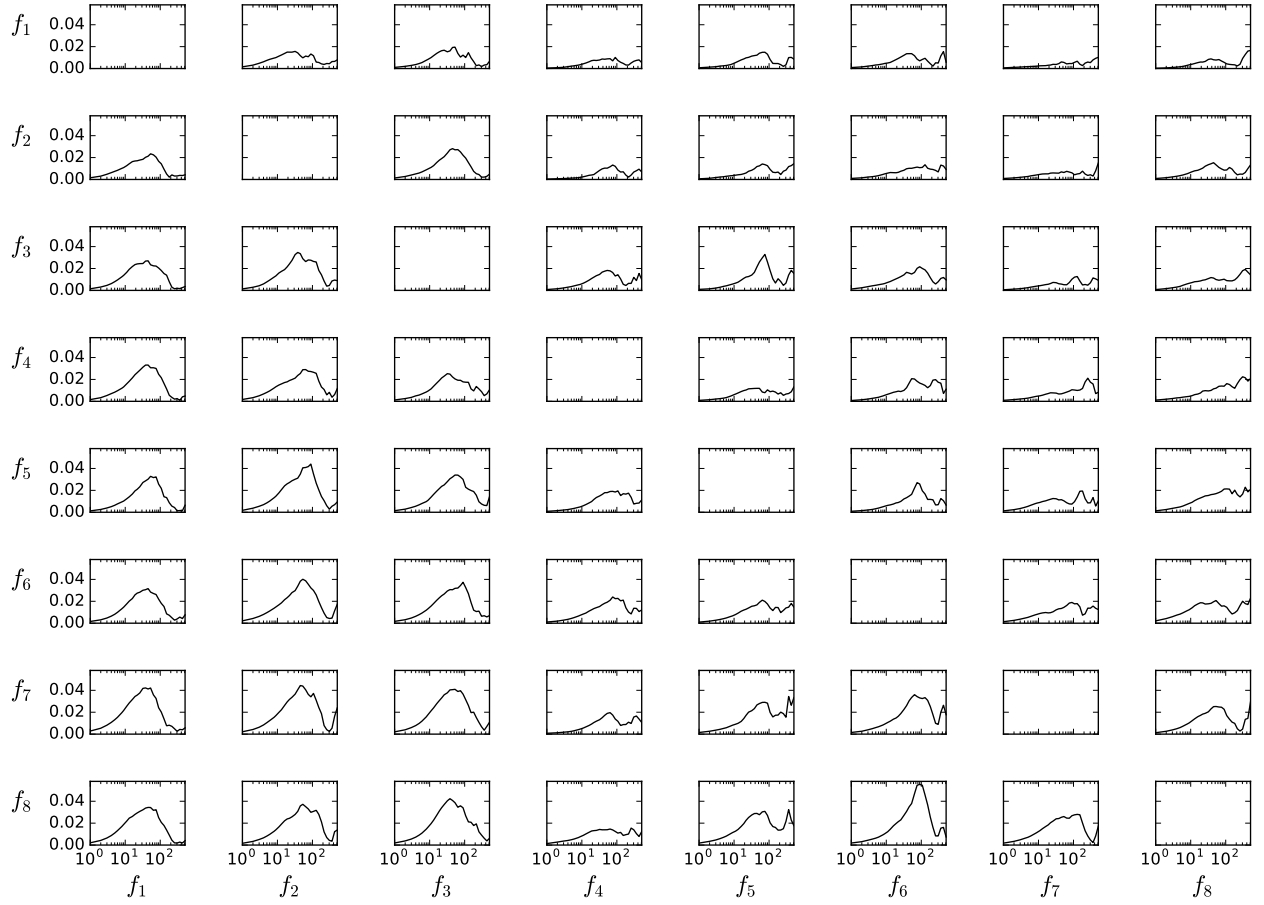


Figure S6. Transfer entropy. We represents functions $\mathcal{T}_{kl}(\tau) = \mathcal{T}_{E_{f_k}^* \rightarrow E_{f_l}^*}(\tau)$ for values of τ in a range between $[1, 2^9]$ (i.e. from 1 minute to 8.5 hours) logarithmically distributed with intervals of $2^{0.25}$. Rows specify the value of f_k while columns specify the value of f_l . For each graph, the vertical axis represents the value of transfer entropy and the horizontal axis the value of τ in minutes.